CHEMISTRY
A European Journal

A Journal of
ChemPubSoc Europe

Accepted Article

Title: Co3O4@Co/NCNT Nanostructure Derived from a Dicyanamide Based Metal-Organic Framework as Efficient Bi-functional Electrocatalyst for Oxygen Reduction and Evolution Reactions

Authors: Nivedita Sikdar, Bharathi Konkena, Justus Masa, Wolfgang Schuhmann, and Tapas Kumar Maji

To be cited as: *Chem. Eur. J.* 10.1002/chem.201704211

Link to VoR: http://dx.doi.org/10.1002/chem.201704211

Supported by
ACES

WILEY-VCH

10.1002/chem.201704211

WILEY-VCH

Co_3O_4@Co/NCNT Nanostructure Derived from a Dicyanamide Based Metal-Organic Framework as Efficient Bi-functional Electrocatalyst for Oxygen Reduction and Evolution Reactions

Nivedita Sikdar,[a],† Bharathi Konkena,[b],† Justus Masa,[b] Wolfgang Schuhmann,[b]* and Tapas Kumar Maji[a]*

Abstract: There has been growing interest in the synthesis of efficient reversible oxygen electrodes for both the oxygen reduction reaction (ORR) and the oxygen evolution reactions (OER) for their potential use in a variety of renewable energy technologies such as regenerative fuel cells and metal–air batteries. Here, we report a bi-functional electrocatalyst derived from a novel dicyanamide based nitrogen rich MOF $\{[Co(bpe)_2(N(CN)_2)]\cdot(N(CN)_2)\cdot(5H_2O)\}_n$ [Co-MOF-1, bpe = 1,2-bis(4-pyridyl)ethane, $N(CN)_2^-$ = dicyanamide] under different pyrolysis conditions. Pyrolysis of the Co-MOF-1 under Ar atmosphere (at 800 °C) yielded a Co nanoparticles embedded N-doped carbon nanotube matrix (Co/NCNT-Ar) while pyrolysis under a reductive H_2/Ar atmosphere (at 800 °C) and further mild calcination yielded Co_3O_4@Co core-shell nanoparticles encapsulated N-doped carbon nanotubes (Co_3O_4@Co/NCNT). Both catalysts show bi-functional activity towards ORR and OER, however, the core-shell Co_3O_4@Co/NCNT nanostructure exhibited superior electrocatalytic activity for both the ORR with a potential of 0.88 V at a current density of -1 mA cm^{-2} and the OER with a potential of 1.61 V at 10 mA cm^{-2}, which is competitive with the most active bi-functional catalysts reported previously.

Introduction

Increased understanding of oxygen electrochemistry will lead to wider use of the most promising clean and sustainable electrochemical energy storage and conversion systems, including regenerative fuel cells and metal-air batteries among others.[1-3] Oxygen electrochemistry entails water oxidation to release molecular oxygen (oxygen evolution reaction (OER)), and the inverse reaction, oxygen reduction to produce water (oxygen reduction reaction (ORR)). The OER is of practical importance in many electrochemical systems like electrowinning,[4] electroplating[5] and photo-electrochemical water splitting,[6] whereas the ORR is fundamentally essential in fuel cells.[7] These reactions involve multi-electron transfer steps with different mechanisms associated with a variety of reaction intermediates, which require improved understanding in order to resolve the kinetic limitations of the reactions. Typically, OER and ORR have been studied and reported separately.

Bi-functional catalysts, capable of driving both reactions, for example in unitized regenerative fuel cells (URFC), demand the development of reliable catalyst materials that are abundant and cheap.[8] Presently, well known catalysts for ORR and OER are precious metals or their alloys, and precious metal oxides.[9-11] Considering the high cost and scarcity of precious metals, a number of alternative earth abundant materials such as transition metal (e.g., Fe, Ni, Co and Mn) oxides,[12-13] sulphides,[14-15] phosphides[16-17] and nitrides/borides[18-19] have been introduced into the field. More recently, nanocarbon materials and their composites have been recognized as very active and stable materials.[20-23] Furthermore, the catalytic properties are improved by introducing heteroatoms like N, B and S which modify the electronic and structural properties of carbon.[24-26] The enhanced performance arises from the electronic structure, conductivity and carbon defects induced by the hetero atoms.[27-28] However, fabrication of efficient bi-functional ORR and OER electrocatalysts need to be further explored for sustainable energy conversion. Thus, new synthetic methodologies are required to develop for fabrication of metal free or non-precious and abundant metal based bi-functional catalysts for reversible oxygen electrodes in unitized regenerative fuel cells or metal-air batteries.[29-30]

Recently, metal–organic frameworks (MOFs) have attracted enormous interest as self-sacrificial templates for the tunable synthesis of metal/metal-oxide encapsulated hierarchical graphitic nanostructures under different pyrolyzing conditions.[31] MOFs are a class of coordination polymers composed of metal ions and organic ligands, and are potential materials for gas storage and separation, luminescence, sensing and catalysis among others.[32-34] The derived materials have shown to be promising in hydrogen storage, sensing, electrochemical capacitors and in lithium-ion batteries.[31] Notably, N-doped nanocarbon frameworks have been demonstrated to be efficient

[a] N. Sikdar, Dr. T. K. Maji
Chemistry and Physics of Materials Unit (CPMU)
Jawaharlal Nehru Centre for Advanced Scientific Research (JNCASR)
Bangalore-560064, Karnataka, India
E-mail: tmaji@jncasr.ac.in
[b] Dr. B. Konkena, Dr. J. Masa, Prof. W. Schuhmann
Analytical Chemistry - Center for Electrochemical Sciences (CES)
Ruhr-University Bochum, 44780 Bochum, Germany
Email: wolfgang.schuhmann@rub.de
†(N. Sikdar and Dr. B. Konkena) These authors equally contributed to this work

Supporting information for this article is given via a link at the end of the document.((Please delete this text if not appropriate))

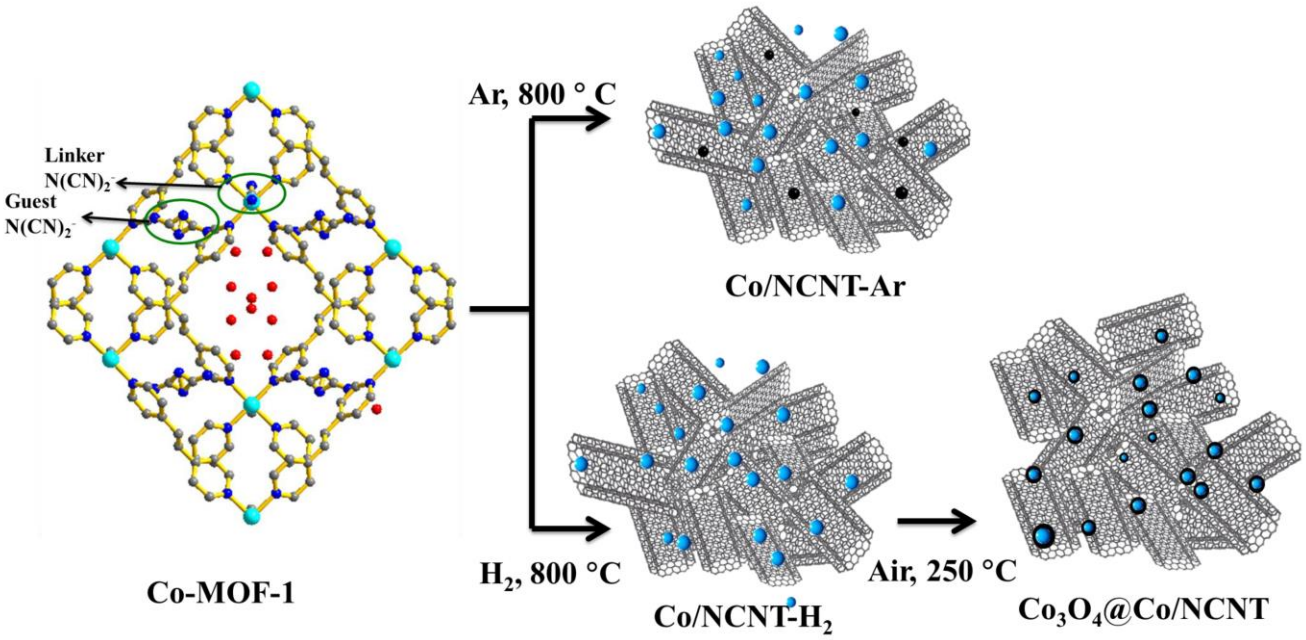

Scheme 1. Schematic of Co-MOF-1 (grey = C, blue = N, red = O, cyan = Co) pyrolysis to prepare MOF derived Co/NCNT-Ar and Co_3O_4@Co/NCNT electrocatalysts under different conditions (blue= Co, black= Co_3O_4).

ORR and OER electrocatalysts.[35-36] However, only a handful of examples of bi-functional electrocatalysts have been reported. A catalyst with low overpotential difference between ORR and OER is of prime importance for application as electrocatalyst for reversible oxygen electrodes. Notably, a subclass of MOFs, zeolitic imidazolate frameworks (ZIFs) such as Ni-ZIF, Co-ZIF, Zn-ZIF, among others, have been utilized as excellent templates for producing metal rich porous N-doped nanocarbon electrocatalysts.[37-39] In a recent report, a Co based core–shell (Co_3O_4@Co) bi-functional electrocatalyst from Co-ZIF was synthesized, where the synergetic effect of the core-shell Co_3O_4@Co structure on the electrocatalytic properties was explained.[40] We envisage that increasing the N-content and graphitic nature of the matrix may decrease the overpotential difference, hence, better catalytic properties. With this assumption, we considered a novel dicyanamide containing porous framework $\{[Co(bpe)_2(N(CN)_2)]\cdot(N(CN)_2)\cdot(5H_2O)\}_n$ [Co-MOF-1, bpe = 1,2-bis(4-pyridyl)ethane), $N(CN)_2^-$ = dicyanamide], reported earlier,[41] as carbonization template. Dicyanamide, being a chemical precursor for *g*-C_3N_4 can be an ideal source of N-doped graphitic matrix, rich in Co-N_4 centers. Coupling of these Co-N_4 moieties with metallic Co cores surrounded with a semiconductive Co_3O_4 shell, is expected to provide superior bi-functional electrocatalytic performance.[40]

Herein, we report for the first time the preparation of a Co and core-shell Co_3O_4@Co nanoparticle containing N-doped carbon nanotube (NCNT) matrix (Co/NCNT-Ar and Co_3O_4@Co/NCNT) as an active and stable bi-functional electrocatalyst from a cheap and easily scalable Co-MOF-1 under different pyrolysis conditions (under Ar, H_2/Ar and mild calcination at elevated temperature) (Scheme 1).[41] We have studied a detailed comparative study with state-of-art catalysts as well and observe that the core-shell Co_3O_4@Co/NCNT showed substantially improved bi-functional catalytic activity and durability comapred to state-of-art benchmark electrocatalysts under similar conditions. Most importantly, the difference between the overpotentials measured at current densities of -1 mA cm^{-2} for the ORR and 10 mA cm^{-2} for the OER did not exceed 0.73 V for the Co_3O_4@Co/NCNT catalyst, suggesting that the core-shell Co_3O_4@Co/NCNT catalyst is one of the best bi-functional OER and ORR catalysts reported so far.

Results and Discussion

In this study, we have deliberately chosen dicyanamide ($N(CN)_2^-$) containing Co^{II}-based two-fold interpenetrated 3D framework $\{[Co(bpe)_2(N(CN)_2)]\cdot(N(CN)_2)\cdot(5H_2O)\}_n$ (Co-MOF-1) (Figure S1-2), reported previously,[41] as a precursor for the synthesis of bi-functional catalysts for reversible oxygen electrodes. This flexible framework showed permanent porosity and high thermal stability. In Co-MOF-1, each metal centre is octahedrally coordinated to four bpe ligands and two $N(CN)_2^-$ anions, resulting in overall Co^{II}-N_6 moieties (Figure S1a). The four bpe linkers are connected through Co^{II} centres to form two dimensional sheets along *ab* plane which is pillared by $N(CN)_2^-$ anions constructing a 3D framework (Figure S1b). Two such 3D frameworks entangle with each other resulting in a porous framework occupied by the $N(CN)_2^-$ ions and water molecules. By this, 24 carbon and 8 nitrogen atoms are present per formula

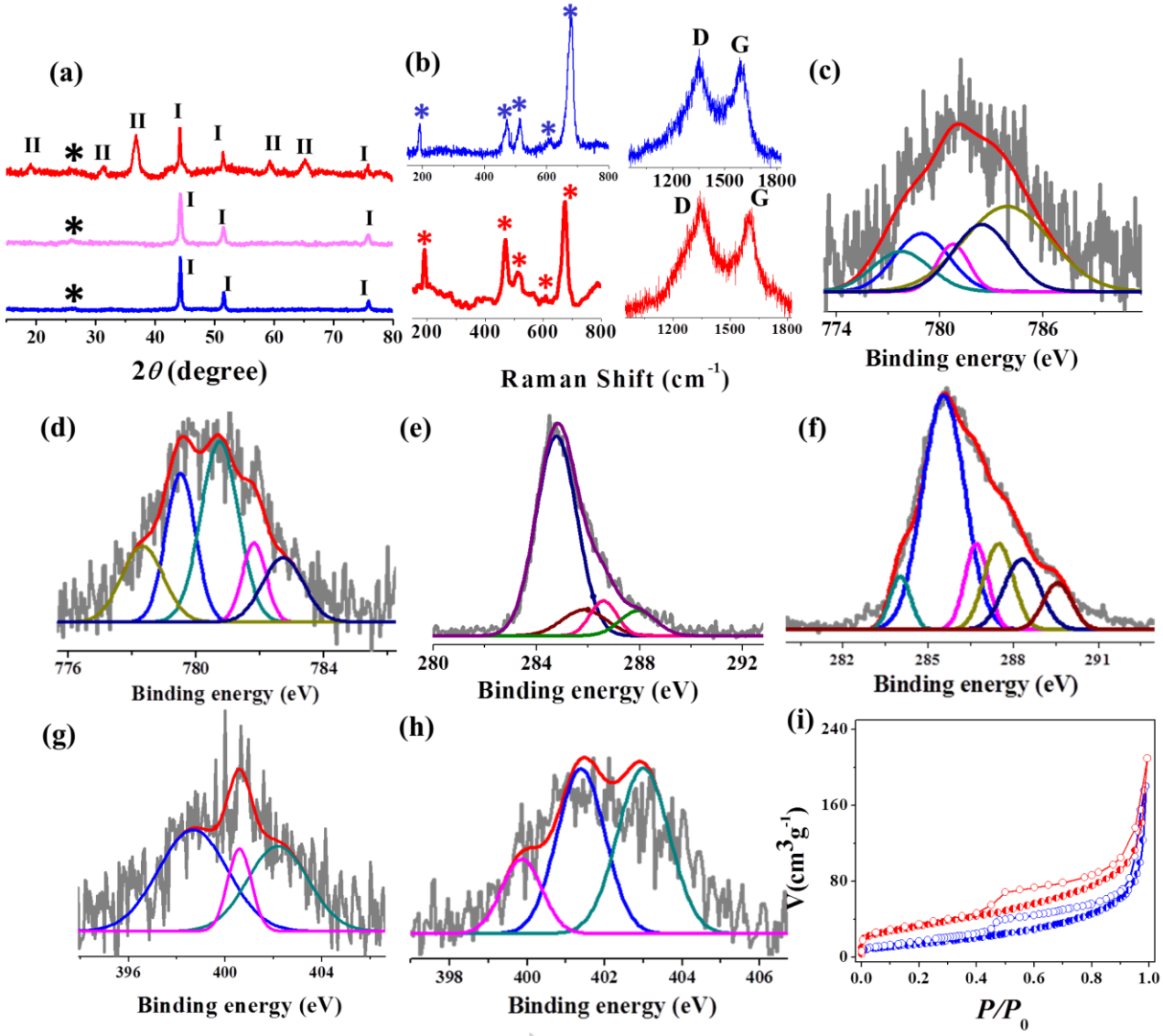

Figure 1. (a) PXRD pattern of Co/NCNT-Ar (blue), Co/NCNT-H_2 (black) and Co_3O_4@Co/NCNT (red); *, I, II denote the graphitic (002) peak, Co peaks and Co_3O_4 peaks, respectively; (b) Raman spectra of Co/NCNT-Ar (blue) and Co_3O_4@Co/NCNT (red) showing Co_3O_4 phase, along with the characteristic D and G bands; (c) Co 2p core level spectrum of Co/NCNT-Ar, and (d) of Co_3O_4@Co/NCNT; (e) C 1s core level XPS spectra of Co/NCNT-Ar and (f) for Co_3O_4@Co/NCNT; (g) N 1s core level XPS spectrum of Co/NCNT-Ar and (h) of Co_3O_4@Co/NCNT; (i) N_2 adsorption isotherms of Co/NCNT-Ar (blue) and Co_3O_4@Co/NCNT (red) at 77 K.

unit of Co-MOF-1. Thus, the high carbon, nitrogen content and the abundant Co^{II}-N_6 centres in Co-MOF-1 encouraged us to pyrolize it under different conditions in order to obtain Co centres embedded porous carbon nitride type matrix in which electrochemically active M-N-C sites are supposed to act as non-precious catalytic sites. Co-MOF-1 was pyrolyzed at 800 °C under continuous Ar and separately under H_2/Ar flow (at 800 °C) for 4 h followed by mild calcination in air at 250 °C for 2 h to obtain Co/NCNT-Ar and Co_3O_4@Co/NCNT, respectively, following a procedure as previously described.[40] The obtained materials were characterized using PXRD, Raman spectroscopy, XPS, FESEM and TEM techniques (Figure 1-2). The broad XRD peak at 2θ = 26.1° in Co/NCNT-Ar is due to (002) reflections suggesting regular graphitic stacking (Figure 1a). All the other peaks are assigned to the crystalline metallic cubic Co phase.[40] The PXRD patterns of the materials obtained on H_2/Ar treatment (Co/NCNT-H_2) and after successive mild air oxidation (Co_3O_4@Co/NCNT) also produce (002) peak of regular graphitic stacking at 2θ of 25.9° 26.0°, respectively. The diffraction peaks at 2θ of 44.1°, 55.5° and 75.9° indicate formation of a crystalline Co phase prior to calcination (Co/NCNT-H_2). Mild calcination in air partially oxidizes Co to a spinel Co_3O_4 phase (Co_3O_4@Co/NCNT) as confirmed from the

10.1002/chem.201704211

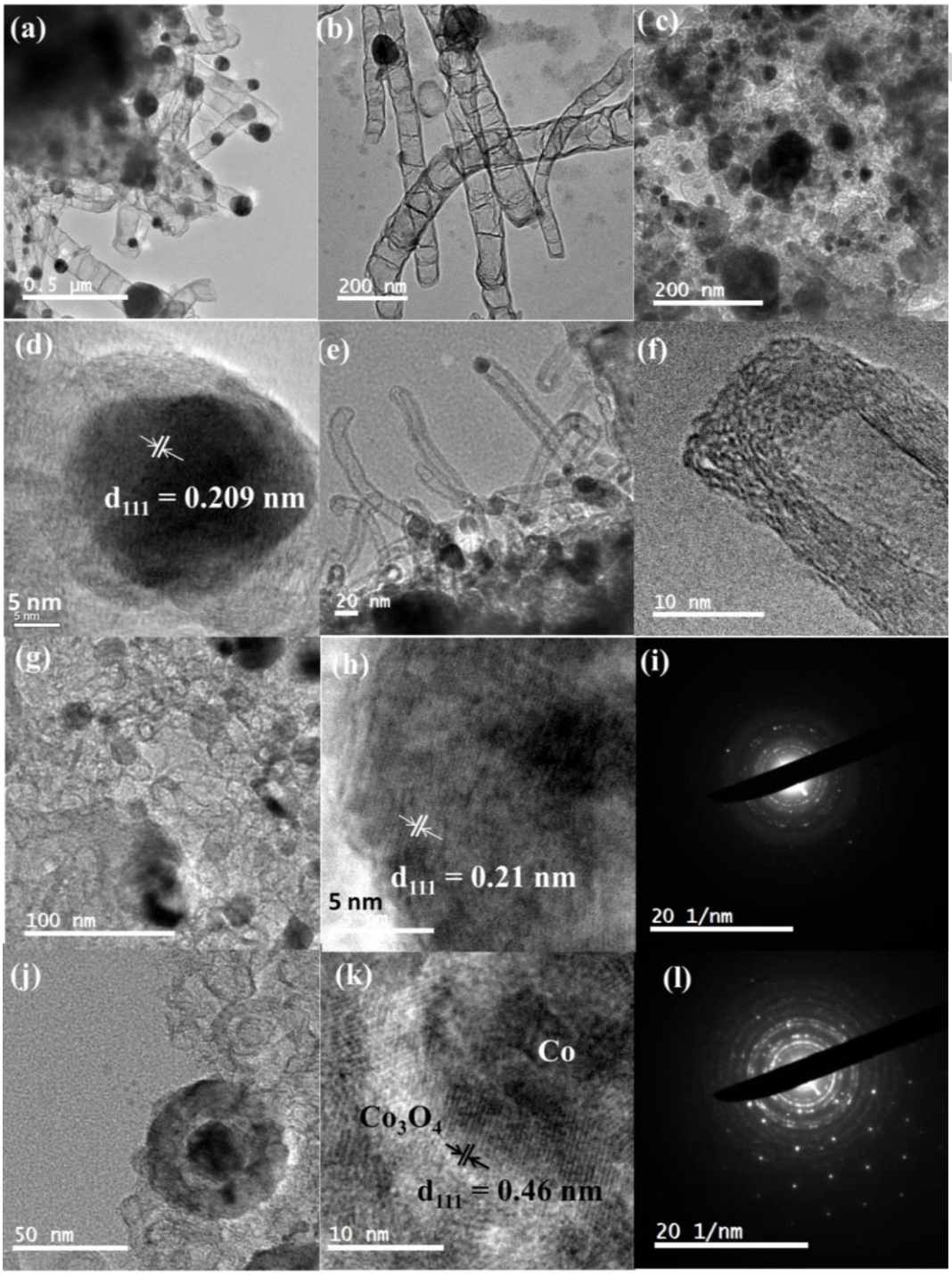

Figure 2. (a) TEM image of Co/NCNT-Ar (b) carbon nanotubes; (c) self-coiled NCNT matrix; (d) HRTEM images of individual Co-nanoparticles wrapped with few layers of graphitic carbon in Co/NCNT-Ar; (e) H_2–pyrolized Co/NCNT-H_2 showing metallic Co nanoparticles dispersed in a NCNT matrix; (f) multi-layers of a single NCNT; (g) self-coiled carbon nanotube NCNT matrix; (h) HRTEM image of one Co nanoparticle; (i) spot-ring SAED pattern of a Co nanoparticle; (j) Co_3O_4@Co core-shell nanoparticle embedded in a NCNT matrix in Co_3O_4@Co/NCNT; (k) HRTEM image of a single Co_3O_4@Co nanoparticle showing lattice fringes; (i) SAED pattern of core-shell Co_3O_4@Co nanoparticle.

newly appearing diffraction peaks at 2θ of 19.0°, 31.4°, 35.8°, 59.3° and 65.2°, consistent with values given in literature.[40] Co /NCNT-Ar, Co/NCNT-H_2 and Co_3O_4@Co/NCNT were further characterized by Raman spectroscopy to evaluate the nature of the graphitic carbon structure (Figure 1b and S3a). The catalysts show the characteristic defect-D band and graphitic-G band at ~1356 cm^{-1} and ~ 1609 cm^{-1} with a $I_G/I_{D\ ratio}$ of 0.85 and 0.91 and 0.87 for Co/NCNT-Ar, Co/NCNT-H_2 and Co_3O_4@Co/NCNT, respectively, demonstrating that a high degree of graphitization have been induced during pyrolysis under Ar and H_2/Ar atmosphere. Notably, Co/NCNT-Ar reveals bands at 192, 471 cm^{-1}, 512 cm^{-1} and 679 cm^{-1}, characteristic of spinel Co_3O_4 phase, suggesting certain amount of non-crystalline Co_3O_4 is present in the NCNT matrix. However, the Co_3O_4 structure has not been not observed in PXRD,.[43] Core-shell catalyst Co_3O_4@Co/NCNT also shows bands at 192 cm^{-1}, 470 cm^{-1}, 510 cm^{-1}, 609 cm^{-1} and 675 cm^{-1}, characteristic of typical Co_3O_4 spinel phase.[44] XPS survey spectra of the samples further confirm the presence of Co, C, N and O (Figure 1c-h). The Co 2p XPS spectrum of Co /NCNT-Ar shows four bands; 778.0 eV band is due to metallic Co $2p_{3/2}$, two bands at 779.0 and 780.7 eV are due to presence of Co_3O_4, 781.9 eV is for Co-N_4 environment and the band at 783.7 eV suggests for $Co(CO)_4$ species, formed due to calcination treatment (Figure 1c).[45] The catalyst obtained after H_2/Ar pyrolization (Co/NCNT-H_2) has Co 2p bands at 778.9, 782.1 and 783.4 for metallic Co, Co-N_4 environment and $Co(CO)_4$, respectively (Figure S3b). The Co 2p spectrum of Co_3O_4@Co/NCNT can be deconvoluted into four peaks, metallic cobalt at 778.0 eV, Co_3O_4 bands at 779.3 and 780.4 eV, the band at 781.9 eV for Co-N_4 environment along with band at 783.3 eV for $Co(CO)_4$ present in the matrix (Figure 1d).[45] The C 1s spectrum of Co /NCNT-Ar consists of C-C/C=C peaks at 284.7 eV, C-O/N-C_{sp2} peak at 285.7 eV, N-C_{sp3} at 286.5 eV and C=O peaks at 287.9 eV (Figure 1e).[46] Similarly, the C 1s spectrum of Co/NCNT-H_2 shows peaks for C-C/C=C, C-O/N-C_{sp2}, N-C_{sp3}, C=O, O-C=O at 285.9, 287.1, 288.3 and 289.4, respectively. The C 1s spectrum of Co_3O_4@Co/NCNT also exhibits peaks centered at 284.1 eV (C-C/C=C), 285.5 eV , 286.7 eV, 287.4 eV, 288.3 eV and 289.6 eV, suggesting the formation of a N-doped graphitic matrix in these cases. Notably, the enhanced C-O peak intensity at 285.8 eV in Co_3O_4@Co/NCNT is probably due to an increased C-O functionalization during the mild calcination process (Figure 1f and S3c). N 1s XPS spectra of Co/NCNT-Ar, Co/NCNT-H_2 and Co_3O_4@Co/NCNT were deconvoluted into three bands at 398.7 eV, 400.6 eV, 401.6 eV; 398.5, 400.8, 401.9 and, and 399.2 eV, 401.1 eV and 402.5 eV attributed to pyridinic, pyrrolic and graphitic N, respectively (Figure 1g-h and S3d).[38] The surface nitrogen content calculated from the XPS measurements was 12.2 % for Co/NCNT-Ar, 11.6 % for Co/NCNT-H_2 and 10.5 % for Co_3O_4@Co/NCN. The Co content determined by ICP-OES was 52.8, 45.7 and 45 wt% for Co/NCNT-Ar, Co/NCNT-H_2 and Co_3O_4@Co/NCNT, respectively.

FESEM and TEM images of Co/NCNT-Ar shows the Co nanoparticles are embedded in a continuous self coiled N-doped carbon nanotube (NCNT) matrix (Figure S4a and 2a-d). The average size of the metal nanoparticles are in the range of ~50-110 nm (Figure 2a-d) and the average diameter of the nanotubes are ~ 50-200 nm. The lattice fringe of the crystalline Co nanoparticle has been found to be ~0.209 nm which corresponds to the {111} of cubic metal structure as observed in the high resolution TEM (HRTEM) image (Figure 2d and S4b). Pyrolysis under H_2 atmosphere also led to the formation of 40-50 nm sized metallic Co nanoparticles in Co/NCNT-H_2, homogeneously embedded in self-coiled dense NCNT matrix (Figure S4c and 2e-i) as revealed from FESEM and TEM images. The lattice fringe of the Co nanoparticle is ~0.21 nm, attributed to the {111} of cubic metal structure as shown in the high resolution TEM (HRTEM) image (Figure 2h).[40] The average diameter of the CNTs was 10-20 nm with the length ranging between 100 and 200 nm. HRTEM confirms the NCNTs to be multiwalled with an average wall thickness of 7-8 nm. In both cases, metal nanoparticles are wrapped with highly graphitic layers of NCNTs and in some cases, these are positioned at the tip of the CNTs. Interestingly, after calcination in air, the Co_3O_4@Co/NCNT formed crystalline core-shell type (50-60 nm sized) Co_3O_4@Co nanoparticles encapsulated in a CNT matrix (Figure 2j-l and S4d). The lattice fringe of the outer shell, i.e. Co_3O_4 is 0.46 nm, attributed to the cubic {111} structure (Figure 2k).[47a] SAED of the Co nanoparticle shows characteristic spot-ring type patterns, whereas, after the formation of core-shell Co_3O_4@Co/NCNT nanoparticles, an additional pattern of Co_3O_4 can be observed (Figure 2l).

Nitrogen adsorption measurements (at 77 K) were performed for deriving the surface area and elucidating the pore structure of the catalysts (Figure 1i, S5). Co/NCNT-Ar, Co /NCNT-H_2 and Co_3O_4@Co/NCNT showed typical type-IV isotherms with BET surface areas of 58, 116 and 118 $m^2\ g^{-1}$, respectively. The pore size distributions of both samples showed a high contribution from *in situ* generated mesopores with dimensions in the range of 2–30 nm calculated using the NLDFT method (Figure S5). The pore volumes of Co/NCNT-Ar, Co/NCNT-H_2 and Co_3O_4@Co/NCNT were 0.219, 0.25 and 0.29 $cm^3\ g^{-1}$, respectively. These data indicate that the high temperature H_2 treatment generated a more porous matrix than pyrolysis in Ar atmosphere.

Electrocatalytic activity and stability

The electrocatalytic activity of as prepared Co/NCNT-Ar, Co/NCNT-H_2 and Co_3O_4@Co/NCNT were examined using cyclic voltammetry (CV) in 0.1 M KOH solution with a catalyst loading of 0.21 mg cm^{-2}. As shown in the CVs (Figure S6, S7a), no appreciable redox peaks were observed for the catalysts in Ar-saturated KOH. In contrast, when the electrolyte solution was saturated with O_2, Co/NCNT-Ar, Co/NCNT-H_2 and Co_3O_4@Co/NCNT showed good activity towards oxygen reduction reaction (ORR) at ~0.87, 0.86 and 0.9 V vs. RHE, suggesting the catalysts to be potential ORR electrocatalysts. Linear sweep voltammograms recorded in the ORR potential region using a rotating disc electrode (RDE) at different rotation speeds are shown in Figure 3 and S7. Co_3O_4@Co/NCNT exhibits remarkable catalytic performance for ORR affording a current density of -1 mA cm^{-2} at comparatively low

overpotentials of 0.88 V (onset potential is 0.93 V vs. RHE) as compared to 0.83 V for Co/NCNT-Ar (onset potential is 0.90 V vs. RHE) and 0.84 V for Co/NCNT-H_2 (onset potential is 0.90 V vs. RHE) at 1600 rpm (Figure 3a). In fact, compared with commercial Pt/C, RuO_2 and IrO_2 nanomaterials applied as reference catalysts within this study, Co_3O_4@Co/NCNT reveals a very close ORR activity to that of commercial Pt/C and a superior performance than RuO_2 or IrO_2. LSV at different speeds were performed showing increasing cathodic current as a function of rotation rate due to the improved mass transport (Figure 3b-c). The kinetic parameters were analysed using the Koutecky-Levich (K-L) equation. As shown in the Figure 3d, the linearity of the K-L plots indicates first-order reaction kinetics with respect to the dissolved oxygen concentration and the average number of electrons transferred (n) per O_2 molecule during the ORR for Co_3O_4@Co/NCNT at different potentials. For Co_3O_4@Co/NCNT, the value of n was calculated to be in the range of 3.92 to 3.96 within the potential range of 0.35 to 0.75 V, indicating the reduction of oxygen predominantly *via* the 4-electron transfer pathway. For Co/NCNT-Ar, and Co/NCNT-H_2 within the same potential range, n was in the range of 2.86-2.57 (Figure S7-8) and 2.55-2.78, respectively. RRDE measurements were further carried out to monitor the hydrogen peroxide yield (% H_2O_2). As shown in Figure 3e and S9,

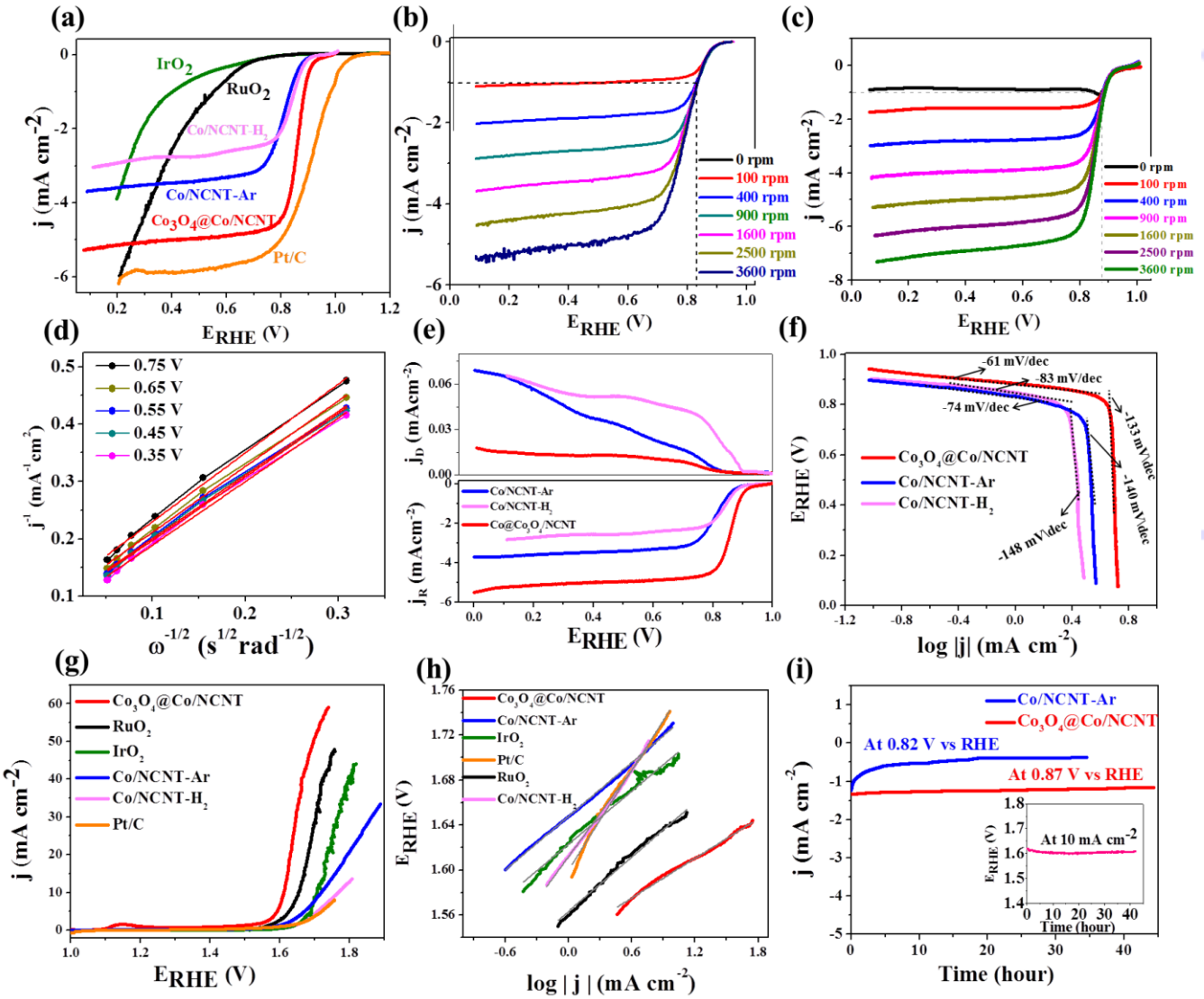

Figure 3. (a) *i*R-corrected linear sweep voltammograms of different electrocatalysts collected at 1600 rpm in O_2-saturated 0.1 M KOH solution; (b) LSV curves recorded at various rotation speeds for Co/NCNT-Ar and (c) for Co_3O_4@Co/NCNT; (d) Koutecky-Levich (K-L) plots at different potentials for Co_3O_4@Co/NCNT; (e) RRDE polarization curves for the ORR at 1600 rpm for Co/NCNT-Ar and Co_3O_4@Co/NCNT; (f) ORR Tafel slopes of Co/NCNT-Ar, Co/NCNT-H_2 and Co_3O_4@Co/NCNT; (g) *i*R-corrected linear sweep voltammograms of different electrocatalysts at 1600 rpm; (h) OER Tafel plots; (i) chronoamperometric stability of Co/NCNT-Ar and Co_3O_4@Co/NCNT; inset shows chronopotentiometric stability of Co_3O_4@Co/NCNT at 10 mA cm^{-2} at 1600 rpm.

the amount of H_2O_2 generated in the entire potential range (0.8 to 0.3 V vs. RHE) decreased from ~54% (maximum value) for Co/NCNT-Ar, 59% for Co/NCNT-H_2 to 1.0% for Co_3O_4@Co/NCNT, respectively, and the calculated electron transfer number for Co_3O_4@Co/NCNT was in the range of 3.97-3.99, while it was 3.19-2.67, 3.05-2.57 for Co/NCNT-Ar, Co /NCNT-H_2, respectively, which are consistent with the results obtained from K-L plots based on RDE measurement. The improved ORR activity of the Co_3O_4@Co/NCNT catalyst is further suggested from the relatively lower Tafel slope of 61 mV dec^{-1}, as compared to 74, 83 mV dec^{-1} for Co/NCNT-Ar, and Co /NCNT-H_2, respectively, indicating faster reaction kinetics (Figure 3f). Notable differences were observed between Co/NCNT-Ar, Co/NCNT-H_2 and Co_3O_4@Co/NCNT, clearly demonstrating that the pyrolization atmosphere plays significant role on the catalytic nanostructure formation. The growth of NCNTs are favoured due to the catalytic effect of *in situ* formed Co nanoparticles.[47b-c] Notably, the surface area of Co_3O_4@Co/NCNT is higher than Co/NCNT-Ar and Co/NCNT-H_2 catalysts prepared in this work. Hence, the well-structured Co_3O_4@Co/NCNT can provide maximum exposure of the active sites from the inner layers to the electrolytes in a better fashion.

Furthermore, the catalysts were investigated with respect to their OER activity as summarized in Figure 3g. The Co/NCNT-Ar and H_2 pylolized Co/NCNT-H_2 nanostructure showed a comparatively much lower activity reaching a current density of 10 mA cm^{-2} at 1.76 and 1.77 V vs. RHE at 1600 rpm, respectively. In contrast, Co_3O_4@Co/NCNT attained 10 mA cm^{-2} at a potential of 1.61 V vs. RHE. This value even surpasses the benchmark catalysts, RuO_2 and IrO_2, exhibiting 1.64 and 1.69 V vs. RHE, respectively, at the same current density. In fact, the ORR and OER activities of this electrocatlyst is comparable to the state-of-art catalysts reported in literature (Table S1). The Tafel slopes for the OER of Co/NCNT-Ar, Co/NCNT-H_2 and Co_3O_4@Co/NCNT in the potential range between 1.55 V and 1.75 V are 80, 128 and 58.7 mV dec^{-1}, respectively, while RuO_2, IrO_2, and Pt/C show Tafel slopes of 78.6 mV dec^{-1}, 80.7 mV dec^{-1}, and 147.8 mV dec^{-1} in the same potential window, indicating that for Co_3O_4@Co/NCNT, the reaction is kinetically substantially faster, making it a highly potent electrocatalyst (Figure 3h). Another well distinguishable feature is the existence of the redox couple at 1.14/1.10 (ΔE = 0.04 vs. RHE), which is due to the formation of Co^{III}/Co^{II} (Figure S10). Thus, Co^{III} species (CoOOH) are identified as key intermediates during OER and the intensity of these bands are very low in Co/NCNT-Ar and Co/NCNT-H_2 (Figure S10).[19,48] Notably, for Co_3O_4@Co/NCNT, the overpotential difference between ORR at a current density of -1 mA cm^{-2} and OER at 10 mA cm^{-2} did not exceed 0.73 V (Figure S11, and Table 1), highlighting the efficiency of Co_3O_4@Co/NCNT in catalyzing both ORR and OER. The sum of the overvoltage between ORR and OER is an important parameter for evaluating bi-functional electrocatalytic activity of reversible oxygen electrodes. Values for this figure of merit, that is the difference between the ORR potential and the potential at a current density of 10 mA cm^{-2} for OER, as proposed by Jaramillo,[9,12] are summarized in Table 1 for different catalysts. Notably, the difference of 0.73 V vs. RHE of the proposed Co_3O_4@Co/NCNT is the lowest among all state-of-art catalysts, and its activity is comparable to recently reported benchmark catalysts (Table S1).[36, 50-55]

MOF pyrolyzed under reductive conditions, i.e. under H_2 atmosphere and at high temperatures (800 ^oC) and further mildly calcined yielded Co_3O_4@Co/NCNT, which showed a substantially enhanced bi-functional activity as compared to only Ar pyrolized Co/NCNT-Ar and H_2 pyrolized Co/NCNT-H_2. We believe that the surface of Co_3O_4@Co in the Co_3O_4@Co/NCNT catalyst at working potentials is different and more active than that of Co/NCNT-Ar and Co/NCNT-H_2 surface. The synergistic interaction between conductive metallic Co cores and the semiconductive Co_3O_4 shell is expected to facilitate faster charge transfer reaction kinetics,[40,49] which is not accessible in the case of Co/NCNT-Ar and Co/NCNT-H_2 catalysts. Interestingly, the activity has been significantly enhanced when the same H_2 pyrolized Co/NCNT-H_2 is being mildly air calcined to prepare core-shell Co_3O_4@Co/NCNT (Table 1). On mild calcination, the overall ORR and OER catalytic activities significantly improve (Figure S11), hence, supporting the high activity of the core-shell electrocatalyst. Another possibility is that annealing of the sample in different atmosphere may cause discontinuities that reveal the underlying defective carbon, which increases the surface area and hence positively impacts on the ORR/OER activity.

Finally, the stability of a given bi-functional catalyst is a critical parameter for its robust operation in any real energy application. The catalysts were thus subjected to chronoamperometric stability tests by continuous polarization at 0.82 V for Co/NCNT-Ar and at 0.87 V for Co_3O_4@Co/NCNT (Figure 3i). The core-shell catalyst Co_3O_4@Co/NCNT is relatively better stable in 0.1 M KOH solution with no significant decline of the current in the course of 30-40 h of continuous polarization. Probably, the strong intimate interaction between Co_3O_4@Co and NCNTs is leading to a highly stable material, particularly, in view of the fact that the oxide particles are embedded in a highly graphitic matrix. Co_3O_4@Co/NCNT also showed excellent stability during OER electrolysis (inset of Figure 3i), suggesting Co_3O_4@Co/NCNT is able to tolerate harsh conditions as a bi-functional catalyst over a long period of time.

Conclusions

In summary, a new $N(CN)_2^-$ rich Co-MOF-1 was chosen as sacrificial precursor for preparing metal nanoparticles embedded in a porous N-doped carboneous matrix at different pyrolysis conditions. Pyrolysis of the MOF under Ar atmosphere (800 ^oC) yielded a mixture of Co/Co_3O_4 nanoparticles distributed in a NCNT matrix. Co-MOF-1 pyrolyzed under a reductive H_2 atmosphere at high temperatures (800 ^oC) and further mildly calcined resulted in Co_3O_4@Co/NCNT, which showed greatly enhanced bi-functional activity in catalysing both ORR and OER as compared to Co/NCNT-Ar. Owing to synergetic interaction between the N-doped CNT matrix and the surface of Co_3O_4@Co embedded in NCNTs, Co_3O_4@Co/NCNT showed excellent bi-functional catalytic activity as well as excellent stability during

both the ORR and the OER. Moreover, the OER activity was even higher than that of commercial RuO_2 and IrO_2. This clearly suggests the potential of nitrogen-rich Co-MOF-1 as novel precursor for the synthesis of Co_3O_4@Co/NCNT as efficient bi-functional catalysts for the ORR and the OER.

Table 1. The bi-functional activity of different catalysts for ORR and OER.

Catalyst	E_{ORR} (V) (E_1) at -1 mA cm^{-2}	E_{ORR} (V) ($E_{1/2}$) half-wave potential	E_{OER} (V) (E_2) at 10 mA cm^{-2}	Tafel slope for OER mV dec^{-1}	ΔE (V) (E_1-E_2)	ΔE (V) ($E_{1/2}$-E_2)
Co/NCNT-Ar	0.83	0.76	1.76	80	0.93	1.39
Co/NCNT-H_2	0.84	0.82	1.77	128	0.93	0.95
Co_3O_4@Co/NCNT	0.88	0.86	1.61	58.7	0.73	0.75
Pt/C	0.99	0.93	-	147.8	-	-
RuO_2	0.56	0.38	1.64	78.6	1.08	1.26
IrO_2	0.42	0.35	1.69	80.7	1.27	1.34

Experimental Section

Synthesis of Co/NCNT-Ar. For the synthesis of Co/NCNT-Ar, 500 mg of Co-MOF-1 was pyrolyzed in an alumina boat under continuous Ar flow at 800 °C (heating rate of 5 °C min^{-1}) for 4 h for complete carbonization.

Synthesis of Co_3O_4@Co/NCNT. The as-synthesised Co-MOF-1 (800 mg) was transferred into an alumina boat and pyrolized under H_2/Ar (5 % H_2 in 95% Ar) flow. The sample (Co/NCNT-H_2) was heated to 800 °C at a heating rate of 5 °C min^{-1} and maintained at this temperature for 4 h. After cooling to room temperature the sample was further calcined at 250 °C in air for 2 h, forming the core-shell Co_3O_4@Co/NCNT structure.

Electrochemical Measurements. For evaluating the electrochemical performances of the pyrolized samples, rotating disk electrode (RDE) voltammetry and rotating ring disk electrode (RRDE) voltammetry were used. All electrochemical measurements were performed using an Autolab PGSTAT12 potentiostat/galvanostat in a conventional three-electrode cell in combination with a Metrohm RDE-2 rotator. The catalyst inks were prepared at a concentration of 5 mg mL^{-1} in a mixture of milliQ water, ethanol, and Nafion (5 wt %, Sigma Aldrich) in the volume ratio of 49:49:2 as dispersion solvent. The mixture was then sonicated for 30 min to obtain a well-dispersed suspension. Glassy carbon electrodes (4 mm diameter) were used as rotating disk electrodes (RDEs). Before experiments, the glassy carbon electrodes were polished on polishing cloth using different alumina pastes (3.0 - 0.05 µm) to obtain a mirror-like surface, followed by ultrasonic cleaning in water. 5 µL of the catalyst ink was drop-cast on a glassy carbon electrode and left to dry overnight under ambient conditions. The catalyst loading for each electrode was 0.21 mg cm^{-2}. A 0.1 M KOH solution was used as electrolyte. The counter and reference electrodes were a platinum foil and an Ag/AgCl/3M KCl electrode, respectively. The reference electrode was calibrated with respect to the reversible hydrogen electrode (RHE). Electrochemical impedance spectroscopy was recorded at the corresponding open circuit potential using an AC perturbation of 10 mV in the frequency range from 50 kHz to 1 Hz. The solution resistance was determined from the resulting Nyquist plot, and later used for ohmic drop correction according to the relation, $E_c = E_m - iR_s$, where E_c is the corrected potential and E_m is the measured potential. All current densities were calculated using the geometric surface area of the electrode. All potentials were rescaled to the pH-independent reversible hydrogen electrode (RHE). The long-term stability was evaluated chronopotentiometrically at a current density of -1 mA cm^{-2} on a graphite rotating disk electrode (5 mm diameter) modified with the catalyst in 0.1 M KOH solution. During the measurements, the electrode was maintained at a rotation of 1600 rpm to avoid accumulation of gas bubbles on the electrode surface. The electrolyte was purged for ~20 min with Ar prior to measurements to determine the background current and later O_2 flow was maintained over the electrolyte throughout the timeframe of the experiment. All measurements were carried out at room temperature. Linear sweep voltammetry (LSV) was performed at rotation speeds of 100, 400, 900, 1600, 2500 and 3600 rpm at a sweep rate of 5 mV s^{-1} .The number of electrons involved in the reduction process was calculated using the Koutecký–Levich (K–L) equation:

$$\frac{1}{j} = \frac{1}{j_L} + \frac{1}{j_K} = \frac{1}{B\omega^{1/2}} + \frac{1}{j_K}$$

$$B = 0.62nFC_o(D_o)^{2/3}\nu^{-1/6}$$

$$j_K = nF\kappa C_o$$

Here, j is the measured current density, j_K and j_L are the kinetic and diffusion-limited current densities, ω is the angular frequency of the RDE

in radians per second, n is the number of electrons involved in the reaction, F is the Faraday constant (96485 C mol^{-1}), D_0 is the diffusion coefficient of O_2 in the electrolyte (1.93 × 10^{-5} $cm^2 s^{-1}$), *v* is the kinematic viscosity of the electrolyte (1.01 × 10^{-2} cm^2 s^{-1}), C_0 is the concentration of O_2 in the electrolyte (1.26 × 10^{-6} mol cm^{-3}) and *k* is the electron transfer rate constant.

Rotating ring disk electrode (RRDE) voltammetry was used to calculate the number of electrons and the amount of H_2O_2 formed during ORR based on the ratio of the disk and the ring current as shown in the equations given below. For the RRDE experiments, the ring electrode was held at a potential of 1.5 V (vs. RHE) to oxidize hydrogen peroxide.

$$n_e = \frac{4\mathrm{I_D}}{\mathrm{I_D} + \frac{\mathrm{I_R}}{\mathrm{N}}}$$

$$\mathrm{H_2O_2(\%)} = \frac{\frac{\mathrm{I_R}}{\mathrm{N}}}{\mathrm{I_D} + \frac{\mathrm{I_R}}{\mathrm{N}}} \times 200$$

N = 0.2678 is the collection efficiency, I_D is the Faradaic disk current, and I_R is the Faradaic ring current.

Acknowledgements

T.K.M. acknowledges DST, (Project No. MR-2015/001019) Govt. of India for financial support. N. S. acknowledges JNCASR and CSIR for scholarship. N. S. acknowledges K. Prasad and S. Ghara for experimental help.

Keywords: Metal/metal-oxide nanoparticles • fuel cells • electrochemistry • oxygen reduction reaction • water oxidation

[1] G. Chen, S. R. Bare, T. E. Mallouk, *J. Electrochem. Soc.* **2002**, *149*, A1092-A1099.

[2] J. S. Lee, S. T. Kim, R. Cao, N. S. Choi, M. Liu, K. T. Lee, J. Cho, *Adv. Energy Mater.* **2011**, *1*, 34-50.

[3] M. Shao, Q. Chang, J. P. Dodelet, R. Chenitz, *Chem. Rev.* **2016**, *116*, 3594-3657.

[4] H. T. Yang , H. R. Liu, Y. C. Zhang, B. M. Chen, Z. C. Guo, R. D. Xu, *Int. J Miner. Metall. Mater.* **2013**, *20*, 986-993.

[5] H. Zhang, H. Ning, J. Busbee, Z. Shen, C. Kiggins, Y. Hua, J. Eaves, J. Davis, T. Shi, Y. T. Shao, J. M. Zuo, X. Hong, Y. Chan, S. Wang, P. Wang, P. Sun, S. Xu, J. Liu, P. V. Braun, *Sci. Adv.* **2017**, *3*, e160242.

[6] A. G. Tamirat, J. Rick, A. A. Dubale, W. N. Su, B. J. Hwang, *Nanoscale Horiz.* **2016,** *1*, 243-267.

[7] X. Ge, A. Sumboja, D. Wuu, T. An, B. Li, F. W. T. Goh, T. S. A. Hor, Y. Zong, Z. Liu, *ACS Catal.* **2015,** *5*, 4643-4667.

[8] M. J. Eslamibidgoli, J. Huang, T. Kadyk, A. Malek, M. Eikerling, *Nano Energy* **2016**, *29*, 334-361.

[9] J. Greeley, I. Stephens, A. Bondarenko, T. P. Johansson, H. A. Hansen, T. Jaramillo, J. Rossmeisl, I. Chorkendorff, J. K. Nørskov, *Nat. Chem.* **2009**, *1*, 552-556.

[10] M. Yagi, E. Tomita, T. Kuwabara, *J. Electroanalyt. Chem.* **200**5, *579*, 83-88.

[11] K. A. Kuttiyiel, Y. Choi, S. M. Hwang, G. G. Park, T. H. Yang, D. Su, K. Sasaki, P. Liu, R. R. Adzic, *Nano Energy* **2015**, *13*, 442-449.

[12] C. C. McCrory, S. Jung, J. C. Peters, T. F. Jaramillo, *J. Am. Chem. Soc.* **2013**, *135*, 16977-16987.

[13] J. Masa, W. Xia, I. Sinev, A. Zhao, Z. Sun, S. Grützke, P. Weide, M. Muhler, W. Schuhmann, *Angew. Chem. Int. Ed.* **2014**, *53*, 8508-8512.

[14] D. Kong, J. J. Cha, H. Wang, H. R. Lee, Y. Cui, *Energy Environ. Sci.* **2013**, *6*, 3553-3558.

[15] Z. Peng, D. Jia, A. M. Al-Enizi, A. A. Elzatahry, G. Zheng, *Adv. Energy Mater.* **2015,** *5*, 1402031-1402038.

[16] L. A. Stern, L. Feng, F. Song, X. Hu, *Energy Environ. Sci.* **2015**, *8,* 2347-2351.

[17] J. Li, J. Li, X. Zhou, Z. Xia, W. Gao, Y. Ma, Y. Qu, *ACS Appl. Mater. Interfaces* **2016**, *8*, 10826-10834.

[18] Y. Zhang, B. Ouyang, J. Xu, G. Jia, S. Chen, R. S. Rawat, H. J. Fan, *Angew. Chem. Int. Ed.* **2016**, *55*, 8670-8674.

[19] J. Masa, P. Weide, D. Peeters, I. Sinev, W. Xia, Z. Sun, C. Somsen, M. Muhler, W. Schuhmann, *Adv. Energy Mater.* **2016**, *6*, 1502313.

[20] Q. Li, R. Cao, J. Cho, G. Wu, *Adv. Energy Mater.* **2014**, *4*, 1301415-1301434.

[21] R. Bashyam, P. Zelenay, *Nature* **2006**, *443*, 63-66.

[22] Y. Liang, Y. Li, H. Wang, H. Dai, *J. Am. Chem. Soc.* **2013**, *35*, 2013-2036.

[23] Y. Ji, L. Huang, J. Hu, C. Streb, Y. F. Song, *Energy Environ. Sci.* **2015**, *8*, 776-789.

[24] H. Wang, T. Maiyalagan, X. Wang, *ACS Catal.* **2012**, *2*, 781-794.

[25] J. Liang, Y. Jiao, M. Jaroniec, S. Z. Qiao, *Angew. Chem. Int. Ed.* **2012**, *51*, 11496-11500.

[26] Y. Zhao, R. Nakamura, K. Kamiya, S. Nakanishi, K. Hashimoto, *Nat. Commun.* **2013**, *4*, 2390.

[27] Y. Zheng, Y. Jiao, J. Chen, J. Liu, J. Liang, A. Du, W. Zhang, Z. Zhu, S. C. Smith, M. Jaroniec, *J. Am. Chem. Soc.* **2011,** *133*, 20116-20119.

[28] Z. J. Jiang, Z. Jiang, *Sci Rep.* **2016**, *6*, 27081.

[29] K. Parvez, S. Yang, Y. Hernandez, A. Winter, A. Turchanin, X. Feng, K. Müllen, *ACS Nano* **2012**, *6*, 9541-9550.

[30] S. Han, D. Wu, S. Li, F. Zhang, X. Feng, *Adv. Mater.* **2014**, *26*, 849-864

[31] K. Shen, X. Chen, J. Chen, Y. Li, *ACS Catal.* **2016**, *6*, 5887-5903.

[32] J. R. Li, J. Sculley, H. C. Zhou, *Chem. Rev.* **2012**, *112*, 869-932.

[33] L. E. Kreno, K. Leong, O. K. Farha, M. Allendorf, R. P. Van Duyne, J. T. Hupp, *Chem. Rev.* **2012**, *112*, 1105-1125.

[34] Y. Cui, Y. Yue, G. Qian, B. Chen, *Chem. Rev.* **2012**, *112*, 1126-1162.

[35] T. Asefa, *Acc. Chem. Res.* **2016**, *49*, 1873-1883.

[36] J. C. Li, P. X. Hou, S. Y. Zhao, C. Liu, D. M. Tang, M. Cheng, F. Zhang, H. M. Cheng, *Energy Environ. Sci.* **2016**, *9*, 3079-3084.

[37] L. Zhang, Z. Su, F. Jiang, L. Yang, J. Qian, Y. Zhou, W. Li, M. Hong, *Nanoscale* **2014**, *6*, 6590-6602.

[38] W. Xia, J. Zhu, W. Guo, L. An, D. Xia, R. Zou, *J. Mater. Chem.* A, **2014**, *2*, 11606-11613.

[39] L. Shang, H. Yu, X. Huang, T. Bian, R. Shi, Y. Zhao, G. I. Waterhouse, L. Z. Wu, C. H. Tung, T. Zhang, *Adv. Mater.* **2016**, *28*, 1668-1674.

[40] A. Aijaz, J. Masa, C. Rösler, W. Xia, P. Weide, A. J. Botz, R. A. Fischer, W. Schuhmann, M. Muhler, *Angew. Chem. Int. Ed.* **2016**, *55*, 4087-4091.

[41] T. K. Maji, R. Matsuda, S. Kitagawa, *Nature Mater.* **2007**, *6*, 142-148.

[42] V. Chabot, D. Higgins, A. Yu, X. Xiao, Z. Chen, J. Zhang, *Energy Environ. Sci.* **2014**, *7*, 1564-1596.

[43] S. H. Johnson, C. L. Johnson, S. J. May, S. Hirsch, M. Cole, J. E. Spanier, *J. Mater. Chem.* **2010**, *20*, 439-443.

[44] M. Rashad, M. Rüsing, G. Berth, K. Lischka, A. Pawlis, *J. Nanomater.* **2013**, 82-88.

[45] K. Artyushkova, S. Levendosky, P. Atanassov, J. Fulghum, *Top Catal*. **2007**, *46*, 263-275.

[46] H. W. Tien, Y. L. Huang, S. Y. Yang, J. Y. Wang, C. C. M. Ma, *Carbon* **2011**, 1550-1560.

[47] (a) H. Jin, J. Wang, D. Su, Z. Wei, Z. Pang, Y. Wang, *J. Am. Chem. Soc.* **2015**, *137*, 2688-2694; (b) Y. Homma, Y. Kobayashi, T. Ogino, J. *Phys. Chem. B* **2003**, *107*, 12161-12164; (c) G. N. Ayre, T. Uchino, B.

Mazumder, A. L. Hector, J. L. Hutchison, D. C Smith, P. Ashburn, C. H. de Groot, *J. Phys.: Condens. Matter* **2011**, *23*, 394201.

[48] H. Y. Wang, S. F. Hung, H. Y. Chen, T. S. Chan, H. M. Chen, B. Liu, *J. Am. Chem. Soc.* **2016**, *138*, 36-39.

[49] X. Liu, M. Park, M. G. Kim, S. Gupta, G. Wu, J. Cho, *Angew. Chem. Int. Ed.* **2015**, *54*, 9654-9658.

[50] (a) W. Xia, R. Zou, L. An, D. Xia, S. Guo, *Energy Environ. Sci.* **2015**, *8*, 568-576; (b) Y. J. Sa, K. Kwon, J. Y. Cheon, F. Kleitz, S. H. Joo, *J. Mater. Chem. A* **2013**, *1*, 9992-10001.

[51] (a) Z. Wen, S. Ci, Y. Hou, J. Chen, *Angew. Chem. Int. Ed.* **2016**, *55*, 6972-6977; (b) T. Maiyalagan, K. A. Jarvis, S. Therese, P. J. Ferreira, A. Manthiram, *Nat. Commun.* **2014**, 5, 3949.

[52] (a) E. Duraisamy, P. Gurunathan, H. T. Das, K. Ramesha, P. Elumalai, *J. Power Sources* **2017**, *344*, 103-110; (b) A. Indra, P. W. Menezes, N. R. Sahrai, A. Bergmann, C. Das, M. Tallarida, D. Schmeißer, P. Strasser, M. Driess, *J. Am. Chem. Soc.* **2014**, 136, 17530–17536.

[53] (a) R. M. Ramsundar, J. Debgupta, V. K. Pillai, P. A. Joy, *Electrocatalysis* **2015**, *6*, 341-340; (b) Z. Wen, S. Ci, Y. Hou, J. Chen, *Angew. Chem. Int. Ed.* **2014**, *53*, 6496-6500; (c) N. R. Sahraie, J. P. Paraknowitsch, C. Göbel, A. Thomas, P. Strasser, *J. Am. Chem. Soc.* **2014**, *136*, 14486–14497.

[54] (a) T. Palaniselvam, B. P. Biswal, R. Banerjee, S. Kurungot, *Chem. Eur. J* **2013**, *19*, 9335-9342; (b) J. Zhang, Z. Zhao, Z. Xia, L. Dai, *Nat. Nanotech.* **2015**, *10*, 444-452.

[55] (a) C. Zhang, M. Antonietti, T. P. Fellinger, *Adv. Funct. Mater.* **2014**, *24*, 7655–7665; (b) T. Y. Ma, J. Ran, S. Dai, M. Jaroniec, S. Z. Qiao, *Angew. Chem. Int. Ed.* **2015**, *54*, 4646-4650; (c) J. Y. Cheon, K. Kim, Y. J. Sa, S. H. Sahgong, Y. Hong, J. Woo, S. D. Yim, H. Y. Jeong, Y. Kim, S. H. Joo, *Adv. Energy Mater.* **2016**, *6*, 1501794.

10.1002/chem.201704211

WILEY-VCH

Entry for the Table of Contents (Please choose one layout)

FULL PAPER

Electrochemically active Co/NCNT-Ar and Co_3O_4@Co/NCNT electrocatalysts are synthesized from a dicyanamide-based self-sacrificial MOF. Co_3O_4@Co/NCNT exhibits excellent bi-functional activity, the difference between the overpotential measured at -1 mA cm^{-2} for ORR and 10 mA cm^{-2} for OER did not exceed 0.73 V. This activity is surpassing that of commercial RuO_2, IrO_2 and Pt/C, and competitive with the most active bi-functional catalysts reported thus

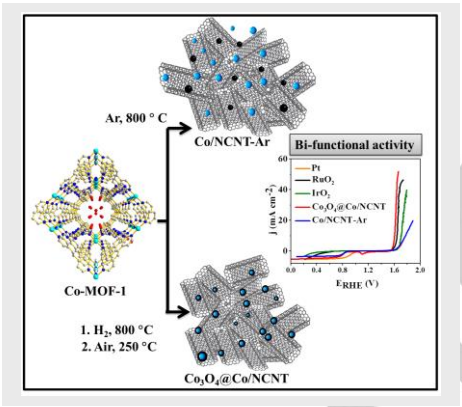

*Author(s), Corresponding Author(s)**

Nivedita Sikdar,[a],† Bharathi Konkena,[b],† Justus Masa,[b] Wolfgang Schuhmann,[b] and Tapas Kumar Maji[a]**

Page No. – Page No.

Co_3O_4@Co/NCNT Nanostructure Derived from a Dicyanamide Based Metal-Organic Framework as Efficient Bi-functional Electrocatalyst for Oxygen Reduction and Evolution